# A Compact Magnetic Directional Proximity Sensor for Spherical Robots

Fang Wu, Luc Maréchal, Akash Vibhute, Shaohui Foong *Member, IEEE,* Gim Song Soh, Kristin L. Wood

***Abstract*— Spherical robots have recently attracted significant interest due to their ability to offer high speed motion with excellent locomotion efficiency. As a result of the presence of a sealed outer shell, its obstacle avoidance strategy has been simply "hit and run". While this is convenient due to the specific geometry of the spherical robots, it however could pose serious issues when the robots are small and light. For portable spherical robots with on-board cameras, a high speed collision with a hard surface may damage the robot or the camera. This paper proposes a novel and compact proximity sensor that utilizes passive magnetic field to detect the ferromagnetic obstacles through perturbation of the magnetic field. Compared with the existing works that utilize the Earth's weak magnetic field as a means of detection, the approach undertaken here seeks to harness the same principle but uses an intelligently designed magnetic assembly. It efficiently amplifies the perturbation and therefore improves the detection performance. The presented method is able to simultaneously determine both the distance and direction of the nearby ferromagnetic obstacles. Both simulation and experimental results are presented to validate the sensing principle and operational performance.**

## I. INTRODUCTION

Spherical robots [1-3] have been a promising research area for decades due to the various advantages based on the specific geometry and locomotion mechanism. Being a closed system, all the components and control units are sealed inside the shell. They are therefore protected from the potential hazardous environment. Rolling itself, is a highly efficient locomotion method, which makes it possible to reduce the battery size and shrink the overall robot size. Moreover, the rolling motion can be easily designed to be omnidirectional [4] without complicating the control mechanism. Its potential applications include homeland security [5], reconnaissance [6] in rescue mission and under water operations [7]. One of the widely claimed advantages of spherical robots is the rapid and natural recovery from collision with obstacles. Unlike the multi-legged robots, it prevents from getting stuck by simply rolling back when hitting an object. While this is acceptable for large and strong-built robots, it is a concern for small scale robots as they typically feature a light-weight and fragile shell to minimize the load.

*Research supported by the SUTD Temasek Laboratories Research Program: Systems Technologies for Autonomous Reconnaissance & Surveillance (STARS) and the SUTD-MIT International Design Centre (IDC).

F. Wu, L. Marechal, A. Vibhute, S. Foong (corresponding author: email: foongshaohui@sutd.edu.sg), G. S. Soh and K. L. Wood are with the Singapore University of Technology of Design, 8 Somapah Road, Singapore 487372.

As shown in Figure 1, the outer shell of small spherical robots are comprised of lightweight thin plastic which allow them to attain high-speed linear motion but unfortunately only provide limited protection from collisions.

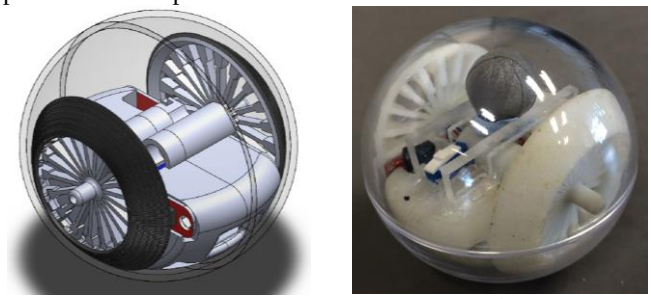

Figure 1. The design CAD model and prototype of VIRGO [6], a spherical robot (Diameter = 8 cm) under development at SUTD.

This issue becomes more problematic when such robotic platforms are used for surveillance. In such applications, these robots are equipped with sensitive payload such as camera and high impact collisions becomes a scenario that should be avoided rather than tolerated. Hence it is necessary to integrate a non-contact proximity sensing system in order to generate the corrective steering commands.

When designing a proximity sensor for spherical robots, the closed structure becomes a hassle. Many common solutions for obstacle detection, including the ultrasonic sensors, require clear line-of-sight. Infrared or laser could penetrate the shell if it is made to be transparent. However, after practical experiments with the infrared sensor, the authors observed a deterioration of its performance due to the abrasion between the shell and the ground, which causes refraction and diffraction of the signals. Electromagnetic-based sensing is more promising as its transmission is unaffected by the plastic shell.

Many urban obstacles such as furniture and walls contain metallic components that create a disturbance on the existing electromagnetic field. It arises from various forms of interactions: induction, capacitive coupling [8, 9] and static magnetic field disturbance. Numerous studies [10-12] have approached the obstacle detection problem using inductive and capacitive sensors. A survey about the commercial inductive and capacitive proximity sensors shows that the sensor size generally increases with the sensing range. Typically, an inductive sensor [13] that has a detection range of 27 mm has a 27.8 mm diameter and 56 mm length, which is too big for a small scale rolling robot. With the size constraints in mind, utilizing the magnetostatic detection and the three-axis magnetometer, which is part of the robot's onboard inertia measurement unit (IMU), is advantageous. While there

are existing researches on using the magnetic anomalies in the earth magnetic field to detect objects, due to the weak response, only large obstacles such as traffic sign post and fire hydrant can be detected [14]. When utilizing a permanent magnet as the magnetic source, magnetic encoders [15] are able to track the motion of a small object such as the gear tooth by creating a local but stronger magnetic field. As a result of replacing the power source with permanent magnets which requires no active power to generate the field, the power consumption can also be reduced. This is extremely suitable for a small and highly compact autonomous robot. Here, this method is extended further by using a pair of permanent magnets to amplify and accentuate the changes in magnetic field. Therefore, directional proximity detection feature can be realized on small spherical robots.

## II. Passive Magnetic-based Proximity Sensor

### A. Principles of Magnetic Field-Based Detection

The Earth's magnetic field on the ground can be approximated to be uniform and parallel to the ground when modelling the Earth as a giant dipole magnet. This field requires no external source and is distorted wherever a ferromagnetic object is present in the vicinity. As shown in Figure 2, an initially uniform magnetic field will deform around a ferromagnetic plate after it is introduced into the environment. The relative concentration of the contour line represents the magnitude of the magnetic flux and it can be seen that the object functions like a weak magnetic source.

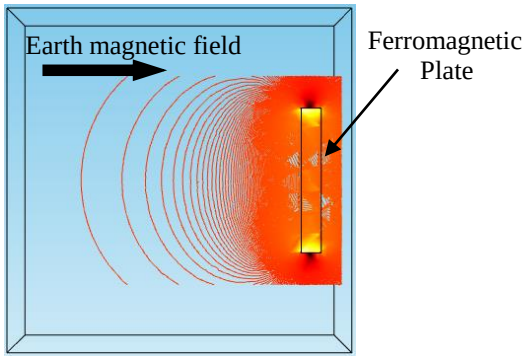


Figure 2. COMSOL simulation of the distorted field due to a ferromagnetic plate when the earth magnetic field is present.

The main drawback with this approach is that the Earth's magnetic field is generally weak (<0.1 mT). Detecting small variations of a weak field is even more challenging. When only the Earth's magnetic field is present, it is often difficult to model the perturbation field induced by a nearby ferromagnetic object. In this case, the field depends not only on the material and geometry of the object, but also on its magnetic orientation relative to the geomagnetic field. Materials and shapes have a proportional relation with the magnitude of the perturbation field, and therefore can be normalized. The magnetic orientation relative to the geomagnetic field remains unknown mainly because the geomagnetic field direction differs from location to location. Various methods have been explored to extract positional information from the small field variations. Some of them [16] sacrificed the direction detecting feature just to achieve a big enough signal. However, in robotic applications, direction detection is paramount for obstacle avoidance and path planning purposes. Therefore, a specially designed passive magnetic field is introduced here to not only magnify the perturbation field, but also detect the approaching direction of a nearby object.

### B. Design Approach and Theoretical Analysis

Taking inspiration from the electrical Wheatstone bridge which allows small resistive changes to be detected, a balanced magnetic flux loop is created through intelligent placement of two permanent magnets. The key idea is to artificially create a magnetic field that possesses a very high spatial gradient. Hence, when a ferromagnetic object is in the vicinity, it will disrupt the magnetic field. Since the magnetic fluxes are continuous and the spatial gradient is high, the instantaneous field variation caused by this disruption will be substantial.

A highly spatially sensitive magnetic field can be created by placing two permanent magnets (PMs) with opposing magnetization close to each other. This technique is employed in the proposed sensor design featured in Figure 3 where a low-powered, compact three-axis magnetic sensor is placed at the midpoint between two PMs. With such a configuration, the magnetic field created by this assembly will deform when a ferromagnetic object approaches the sensor, as shown in a cross-sectional view of a numerically computed magnetic field in Figure 4.

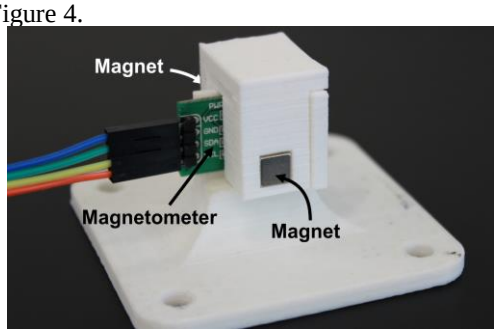


Figure 3. Proposed sensing system comprising of a magnetometer placed between and two permanent magnets (PMs).

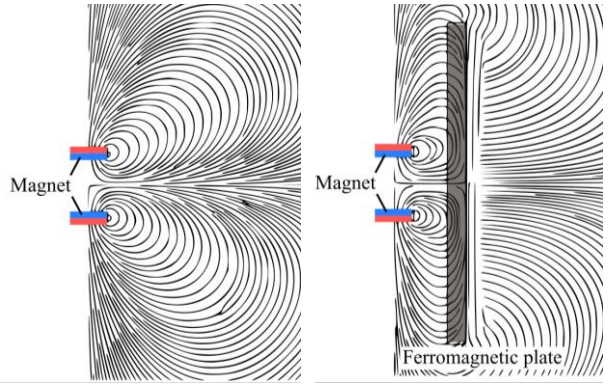


(a) Without obstacle (b) With obstacle

Figure 4. COMSOL simulation of variation of the magnetic flux between the two opposing PMs due to a ferromagnetic obstacle.

Due to the presence of the ferromagnetic plate and its high permeability compared to air, the magnetic flux lines are concentrated towards the sensor. As the field is continuous and has a high spatial gradient, even small object causes a strong disturbance in the magnetic flux loop. Therefore, when proposed configuration in Figure 3 is used as a proximity

sensor, the response in terms of magnetic flux density will be amplified and detected by the magnetometer. Because this interaction is unique, theoretical understanding of the perturbation in the magnetic field will allow determination of the spatial pose (bearing & distance) of the object that causes this perturbation.

The deformation of the magnetic field due to the object would depend on the material, object size, approaching angle, and the distance between the magnets and object. To simplify the analysis, the material permeability is assumed to be infinite and the object size is infinitely large. Then, a 2D model of the resultant magnetic field due to the interaction between the PMs and the object can be analytically built using the magnetic charge model and the image method. As presented in Figure 5(a), two square permanent magnets are located along their magnetization axis with opposite magnetization direction.

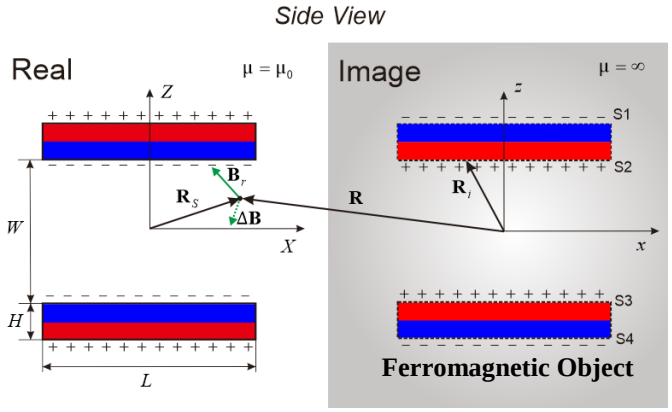


(a) Object approaching along the *X*-axis ($\alpha$=0)

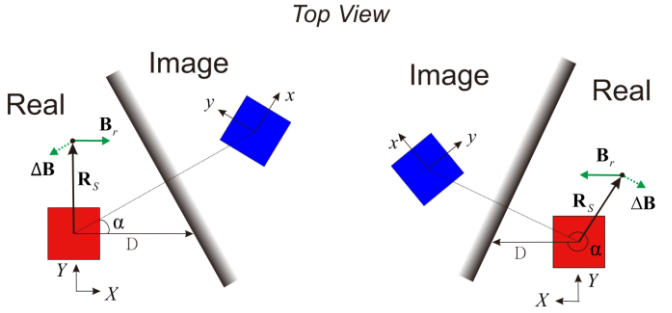


(b) Object approaching with nonzero $\alpha$ angles

Figure 5. Top and side schematics of the sensing assembly. Red and blue surfaces are the 'north' and 'south' poles respectively.

The width and height of the magnets are represented by *L* and *H*, and the distance in-between is expressed as *W*. For clarification purpose, two coordinate systems *X*-*Y*-*Z* and *x*-*y*-*z* are fixed at the central point of the real magnets and image magnets respectively. The *X*(*x*)-axis is in parallel to the magnet surface and the *Z*(*z*)-axis is coincident with the magnetization axis. The magnetic charge model calculates the positive and negative surface charges as the dot product of the magnetization and the surface normal vector, represented by plus and minus signs in Figure 5(a). The magnetic field is then computed by integrating the elementary contribution from the surface charges with respect to the pole area. To account for the magnetic effect due to the object, the material boundary is replaced with the image sources, which in this case are magnetic charges of similar strength and opposite sign.

In Figure 5(a), for ease of illustration of the image method, the approaching direction of the object is parallel to the *X*-axis and in this case the *xyz* coordinate system will be parallel to the *XYZ* coordinate system. In actual applications, it is more common that the objects would approach with a certain angle instead of being parallel, as shown in Figure 5(b). The location of the image magnetic charges will depend on the approaching angle $\alpha$ and the separation distance *D* between the magnets and the obstacle. In addition, the orientation between the *xyz* coordinate system and *XYZ* coordinate system will also depend on the approaching angle. As illustrated in Figure 5, the measured field at any point in space consists of the contribution from the 'real' PMs ($\mathbf{B}_r$) and $\Delta\mathbf{B}$, which is due to the introduction of the object that is represented by the image magnetic charges. The magnetic field due to the image magnetic charges can be computed first with the magnetic charge model in the *xyz* coordinate system and then transformed to the *XYZ* coordinate system via the transformation matrix. The change in the magnetic field due to the image method can be expressed as

$$\Delta\mathbf{B} = \mathbf{B}_i = \mathbf{T} \times \frac{\mu_0}{4\pi}\left( \oint_{S1+S4} \frac{-\sigma_i(\mathbf{R}-\mathbf{R}_i)}{|\mathbf{R}-\mathbf{R}_i|^3} dS + \oint_{S2+S3} \frac{\sigma_i(\mathbf{R}-\mathbf{R}_i)}{|\mathbf{R}-\mathbf{R}_i|^3} dS \right) \tag{1}$$

where $\mathbf{T} = \begin{bmatrix} \cos 2\alpha & -\sin 2\alpha & 0 \\ \sin 2\alpha & \cos 2\alpha & 0 \\ 0 & 0 & 1 \end{bmatrix}$, which accounts for the transformation matrix between the real coordinate system and image coordinate system; $\sigma_i$ represents the image magnetic charge, which is a constant value when assuming the magnetization of the magnet is constant; $\mathbf{R}$ and $\mathbf{R}_i$ represent the location of the field and image charges in the *xyz* coordinate system, as shown in Figure 5; S1, S2, S3 and S4 refers to the surface areas of the image magnets poles.

By rearranging the integration operator, Equation (1) can be reformed as below:

$$\begin{aligned} \Delta\mathbf{B} = \mathbf{T} \times \frac{\mu_0}{4\pi}\Big( & \oint_{S1+S4} \frac{-\sigma_i \mathbf{R}}{|\mathbf{R}-\mathbf{R}_i|^3} dS + \oint_{S2+S3} \frac{\sigma_i \mathbf{R}}{|\mathbf{R}-\mathbf{R}_i|^3} dS \\ & + \oint_{S1+S4} \frac{\sigma_i \mathbf{R}_i}{|\mathbf{R}-\mathbf{R}_i|^3} dS + \oint_{S2+S3} \frac{-\sigma_i \mathbf{R}_i}{|\mathbf{R}-\mathbf{R}_i|^3} dS \Big) \end{aligned} \tag{2}$$

Due to the symmetric structure, the last two terms become null. Equation (2) can be further simplified as below:

$$\Delta\mathbf{B} = \frac{\mu_0 \sigma_i \left( \oint_{S2+S3} \frac{1}{|\mathbf{R}-\mathbf{R}_i|^3} dS - \oint_{S1+S4} \frac{1}{|\mathbf{R}-\mathbf{R}_i|^3} dS \right)}{4\pi} (\mathbf{T} \times \mathbf{R}) \tag{3}$$

In this expression, the scalar coefficients does not affect the direction of $\Delta\mathbf{B}$, which is only dependent on $\mathbf{T}\times\mathbf{R}$. As $\mathbf{T}$ describes the transformation matrix from the *x*-*y*-*z* system to the *X*-*Y*-*Z* system and $\mathbf{R}$ refers to the location of the field in the *x*-*y*-*z* coordinate system, $\mathbf{T}\times\mathbf{R}$ also represents the vector pointing from the center of the image magnets to the field location, expressed in the *X*-*Y*-*Z* coordinate system. As illustrated in Figure 5(b), the center of the image magnets can be expressed in the *X*-*Y*-*Z* coordinate system as $\begin{bmatrix} 2D\cos\alpha\cos\alpha & 2D\cos\alpha\sin\alpha & 0 \end{bmatrix}^{\mathrm{T}}$. With this expression, the normalized field variation can be expressed as follows:

$$\frac{\Delta \mathbf{B}}{|\Delta \mathbf{B}|} = \frac{\mathbf{R}_S}{|\mathbf{R}_S|} - \begin{bmatrix} \cos\alpha \\ \sin\alpha \\ 0 \end{bmatrix} \quad (4)$$

where $\mathbf{R}_S$ represents an arbitrary field location (in this case, the location of the magnetic field sensor) in the *X-Y-Z* coordinate system. Hence, when $\mathbf{R}_S = [0 \quad 0 \quad 0]^T$, the approaching angle can be easily computed from the normalized field variation as below.

$$\alpha = \arctan\left(\frac{\Delta B_Y}{\Delta B_X}\right) \text{ when } \mathbf{R}_S = [0 \quad 0 \quad 0]^T \quad (5)$$

This equation implies that when the sensor is placed at the exact central point between the two magnets, the variation field due to a ferromagnetic object will simply point towards the object's location. Although the derivations above are done under the assumption that the object is infinitely large and with infinite permeability, the outcome remains true for finite object. In addition, for small spherical robots, most obstacles will be much larger than the robot itself. As long as the object is symmetrical with respect to the *XY* plane, it is expected that the variation magnitude decreases while the normalized vector remains to be as (4). Experiments using finite objects of different sizes are presented further to validate the performance.

## III. Numerical Simulations

### A. Theoretical Field Analysis

With the simulation parameters in Table 1 based on actual magnets, the theoretical change in magnetic flux density at $\mathbf{R}_S$ due to an introduction of a ferromagnetic object (governed by *D* and $\alpha$) can be computed using Equation (1) and visually presented in Figure 6. The results in Figure 6 are subdivided into positive and negative α values and the changes in measured magnetic field are decomposed into *X* and *Y* components for ease of comparison.

Table 1. Simulation parameters

| | |
|---|---|
| Width of the magnet (*L*) | 0.64 cm |
| Height of the magnet (*H*) | 0.16 cm |
| Distance between the two magnets (*W*) | 2 cm |
| Surface magnetic field of the magnets ( $B_S$ ) | 0.3032 T |
| Sensor location ( $\mathbf{R}_S$ ) | $[0 \quad 0 \quad 0]^T$ |

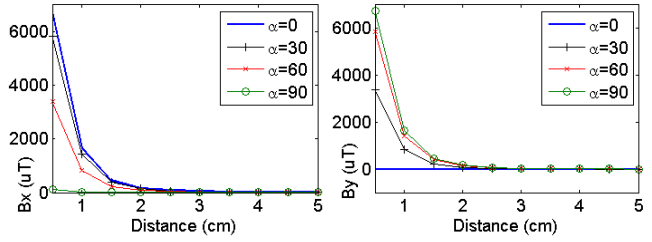


(a)$B_X$ vs *D* when $\alpha > 0$ (b) $B_Y$ vs *D* when $\alpha > 0$

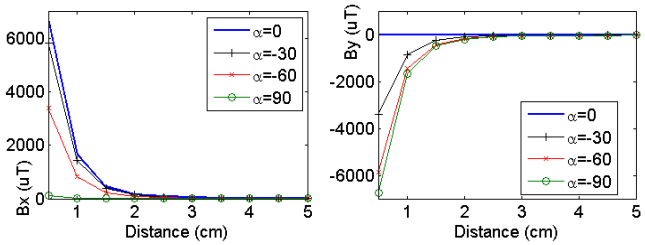


(c) $B_X$ vs *D* when $\alpha < 0$ (d) $B_Y$ vs *D* when $\alpha < 0$

Figure 6. Change in measured magnetic field at $R_S$ due to objects at various *D* and $\alpha$ (presented in degrees) values.

As depicted in Figure 6, the magnitudes in both components decreases with the distance *D*. When α is positive, both $B_Y$ and $B_X$ are positive values; when α is negative, $B_X$ is still positive value while $B_Y$ is negative. For each distance, the approaching angles can be computed directly from the expression in (5). Although, as expected for a constant α, both $B_X$ and $B_Y$ decrease with increasing separation distance, the numerical ratio between $B_X$ and $B_Y$ is maintained which allows determination of the approaching angle. To determine the separation distance, the total magnitude of $B_X$ and $B_Y$, which is independent of α, can be used. The approaching angle does change $B_X$ and $B_Y$ but because magnetic field is axis-symmetric, the total magnitude is unchanged and allows determination of the separation distance of the object from the PMs. It is noted that a typical low-cost magnetic sensor (Freescale MAG3110) has a resolution of 0.1 μT and based on the simulated values in Figure 6, would be able to detect changes in the magnetic field due to an object that is up to 4 cm away, which is more than 6 times the characteristic length of the magnet.

### B. Field Spatial Sensitivity Analysis

Due to the symmetric nature of the magnetic field between the 2 PMs, the ideal location of the sensor would be at the geometric midpoint between the 2 PMs. However due to difficulty in exactly placing the sensor at this precise location and bearing in mind manufacturing imperfections of magnetic sensors, it is important to explore the sensitivity of this effect on the measured magnetic field. The commercial software COMSOL Multiphysics (Burlington, MA, USA) is used to compute the numerical magnetic field distribution between the two permanent magnets and the simulation parameters are listed in the Table.1. In absence of ferromagnetic object around the PMs, the magnetic field distribution in the *X* and *Z* axis are shown in Figure 7(a) and 7(b) respectively. $B_Y$ is not shown as it is similar to $B_X$ field due to axis-symmetry). Both figures show that the measured magnetic field will deviate from 0 μT the further the sensor is displaced from origin (optimal). When a ferromagnetic object is introduced at *D*=2 cm and zero approaching angle (α=0), the corresponding change in the magnetic field in both the *X* and *Z* axis are shown in Figure 7(c) and 7(d) respectively. From Figure 7(c), it can be seen that if the sensor was displaced towards the ferromagnetic object, the magnitude of $\Delta B_X$ (and $\Delta B_Y$ ) will be larger, which is actually advantageous. However, this change is much less than the increase in absolute magnetic field ($B_X$ and $B_X$) without the ferromagnetic object. Hence, with this analysis, although the system is sensitive to spatial

location of the sensor, it is not too significant compared to the instantaneous change in the magnetic field caused by introduction of the object. Although moving the sensor towards the object may seem to increase sensing performance, this requires the direction of the object to be known because if the object approach from the opposite direction, it will lower the field response. What's more, when considering the signal/noise ratio between the variation and the absolute field, the central point is the optimum location for the sensor.

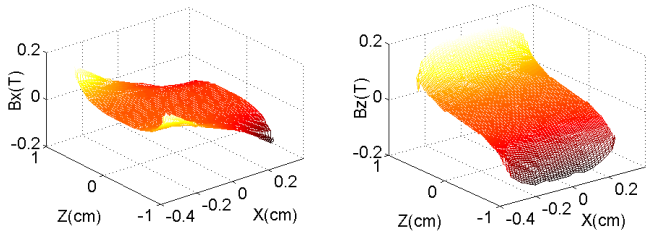


(a) $B_X$ (b) $B_Z$

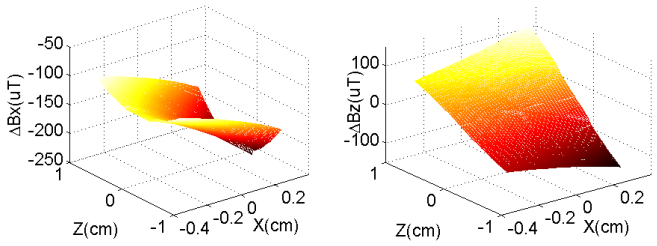


(c)Variation of $B_X$ due to the ferromagnetic object (d)Variation of $B_Z$ due to the ferromagnetic object

Figure 7. Spatial positional sensitivity.

## IV. Experimental Investigation

The performance of the proposed sensing system is experimentally evaluated using a DENSO industrial robot VS068 that provides high positioning accuracy of a ferromagnetic object, which is attached on the end-effector of the robotic arm. The experimental setup is shown in Figure 8, where the sensing assembly is fixed on a non-ferromagnetic table and is partially enclosed by a hemispheric plastic shell that simulates the actual enclosure of a spherical robot. A steel cube of 8cm length is used as the ferromagnetic object and is positioned accurately around the sensing assembly to simulate obstacles with various combination of separation distance $D$ and approaching angle $\alpha$. The parameters of the sensing assembly matches the details presented in Table 1 and the sensor employed is the Freescale MAG3110 three-axis magnetometer, which has a full scale range of ±1000 μT and resolution of 0.1 μT. To extract the field measurements by the MAG3110, an Arduino Uno is used as an interfacing device for data acquisition which communicates with the MAG3110 via I2C.

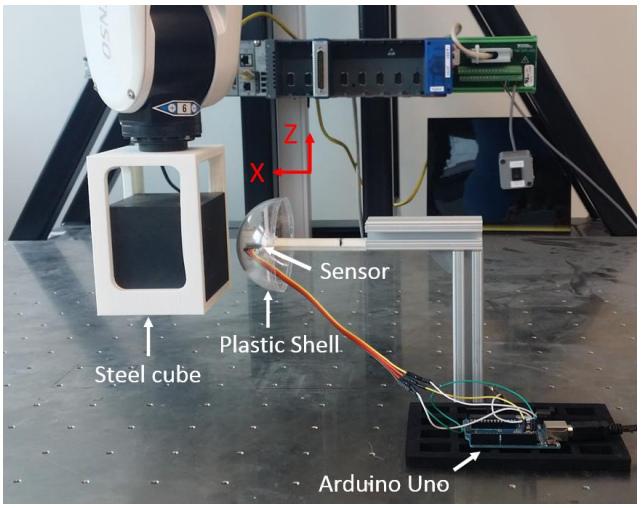


Figure 8. Experimental setup

### A. Signal Amplification

One of the advantages of the proposed sensor over the use of the earth magnetic field is that the magnetic field is magnified near the sensor when an object is in the vicinity. To validate this feature, a steel cube of 8 cm length is moved within a 5 cm by 10 cm surface along the *x*-axis of the sensor, as shown in Figure 8. A step size of 1 mm is used for the robot position and for each location, ten measurements are taken and averaged to reduce the random noise. The scanning process is first conducted around the proposed sensor, which consists of the magnetometer and two permanent magnets. And then the similar trajectory is rendered around the magnetometer only, in which case the earth magnetic field is present. To remove the magnetic effects of the robotic arm, a duplicate scanning process without the steel cube is conducted and the measurements are subtracted from the measurements with the steel cube. The results are shown as below in Figure 9.

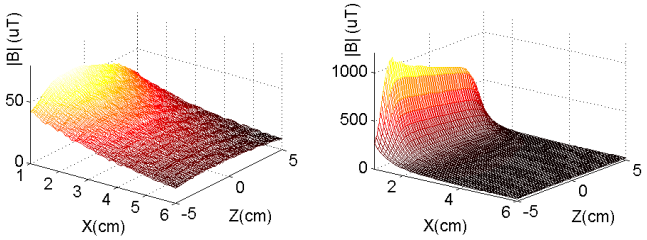


(a)Effect of the object on the Earth's magnetic field (b)Effect of the object on the designed magnetic field

Figure 9. Comparison of the field variation between using only the Earth's magnetic field and amplified field for object detection.

When only the earth magnetic field is present, the maximum disturbance due to the ferromagnetic object is noticeably about 60 μT when the object is closest to the sensor. By contrast, when the proposed sensing system is used where the opposing magnets are used to generate a magnetic field with high gradient, the maximum disturbance due to the ferromagnetic object is up to 1000 μT, which is about 20 times of the one using Earth's magnetic field. Therefore it is experimentally validated that the proposed sensing system will be more sensitive to approaching ferromagnetic objects compared to just using the Earth's magnetic field.

### B. *Ferromagnetic Object Detection & Evaluation*

To validate the direction detection feature of the sensing system, three different paths are conceived for experimental testing as shown in Figure 10. The three paths selected are with approaching angles positive 45, zero and negative 45 degrees respectively. These specific angles are selected due to its capability to represent and simulate the entire frontal area of the sensor. And the effect of objects approaching in the rear area can be reasonably predicted since the sensor configuration is bilaterally symmetric. The axes of the sensor are indicated as $B_X$ and $B_Y$ in shown in Figure 10. A step size of 7 mm is used and due to the sensor geometry, the closest distance between the sensor center and the cube surface is 1.5 cm. For each location, 10 measurements are taken and averaged to remove the random noise. Steel cubes with different dimensions (Small: 2.5×2.5×2.5 cm, Large: 8×8×8 cm) are used as the approaching objects. The experimental measurements of the magnetic field are shown in Figure 11.

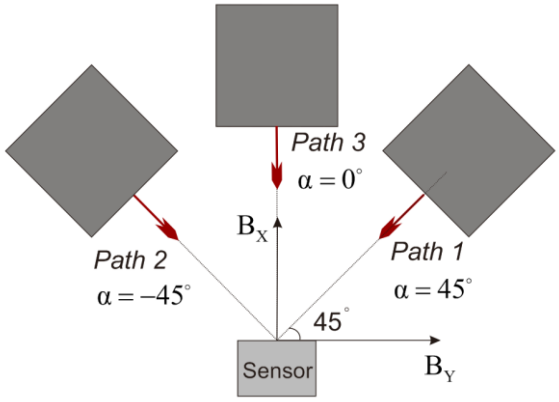


Figure 10. Top view of all three paths to test directional detection.

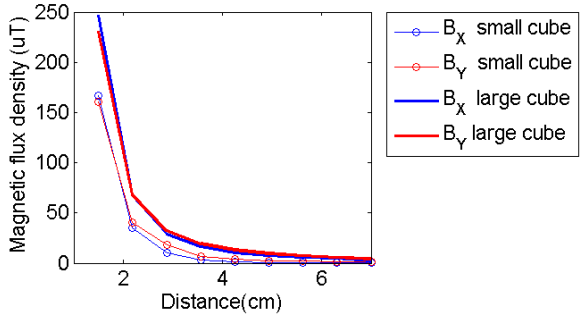


(a) Measurements along the Path 1

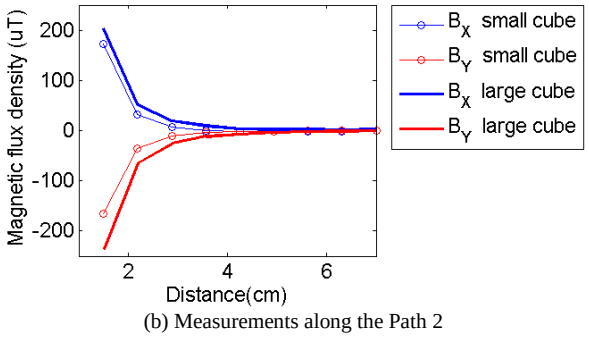


(b) Measurements along the Path 2

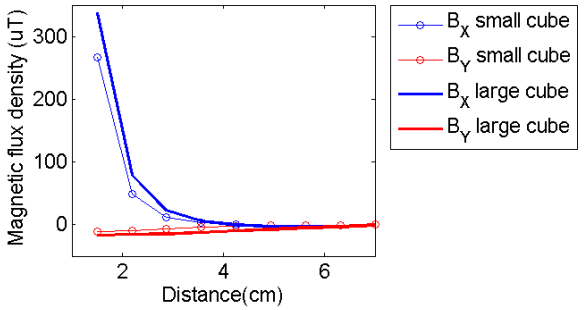


(c) Measurements along the Path 3

Figure 11. Sensor measurements from all three paths using a small and large cubic ferromagnetic object

From the results, it is shown that when the object is moving along Path 1, no matter the size of the cube, both $B_X$ and $B_Y$ are positive values. For the small cube, the maximum value of $B_X$ is 167 μT and that of $B_Y$ is 160.6 μT. For the large cube, the maximum value of $B_X$ is 246.5 μT and that of $B_Y$ is 231.1 μT. And when the object is moving along the Path 2, $B_X$ has a positive value while $B_Y$ is negative. For the small cube, the maximum value of $B_X$ is 172.5 μT, and the minimum value of $B_Y$ is -165.4 μT. For the large cube, the maximum value of $B_X$ is 203.6 μT and the minimum value of $B_Y$ is -234.9 μT. When the object is moving straight towards the sensor, $B_X$ has a much higher value than $B_Y$. For the small cube, the maximum value of $B_X$ is 267.1 μT and that of $B_Y$ is only 10.8 μT. For the large cube, the maximum value of $B_X$ is 337.3 μT and that of $B_Y$ is 15.9 μT.

In all three paths and both objects, the ratio of the magnetic field measurements in $B_X$ and $B_Y$ can be used to determine the approaching angle of the object. Using the data in Figure 11, the estimated approaching angle of the object (which is independent of the object size) can be determined using Equation (5). The estimated angles for all three paths and both sizes are summarized in Table 2 and compared to the actual angle, which is directly measured from the pose of the robotic arm. Majority of the errors were less than 1% with the largest angular error at 1.13% occurring at Path 2 when the larger cube was used.

Table 2. Estimated approaching angle

| Small cube (2.5×2.5×2.5 cm) | | | |
|---|---|---|---|
| Approaching angle (deg) | 0 | 45 | -45 |
| Estimated angle (deg) | -2.31 | 43.88 | -43.80 |
| Error ( $\Delta\alpha$ / 360 ) | 0.64% | 0.31% | 0.33% |
| Large cube (8×8×8 cm) | | | |
| Approaching angle (deg) | 0 | 45 | -45 |
| Estimated angle (deg) | -2.69 | 43.15 | -49.08 |
| Error ( $\Delta\alpha$ / 360 ) | 0.75% | 0.51% | 1.13% |

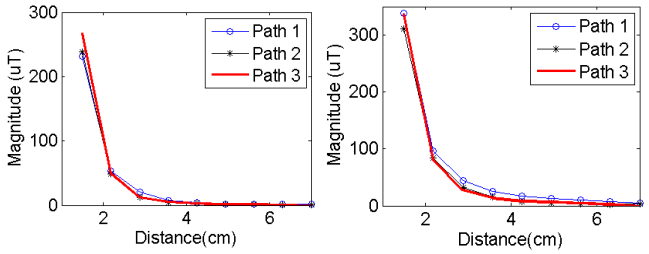


(a) Results with small cube (b) Results with large cube

Figure 12. Magnitude of the magnetic flux disturbance as a function of separation distance *D*.

To show that the total magnitude can be used to infer separation distance between the object and sensing assembly, Figure 12 shows the change in total magnetic flux density when the small and large cubic objects are at various separation distance from all three paths. It is apparent from the results that despite the significant change in the approaching angles, the total magnetic field for the same separation distance $D$ is unchanged. This characteristic will allow the sensing system to detect the distance of an object at any approaching angle. By combining the use of both the ratio of $B_X$ and $B_Y$ as well as the total magnitude, the sensing system can be used to determine an object's directional proximity as well as the distance to the object.

## V. Conclusions

A directional proximity sensor using passive magnetic fields has been conceived and designed for spherical robots. Both the simulation and experimental results demonstrate that the sensing system can not only detect the presence of a nearby ferromagnetic object, but also provide important information about the object approaching direction, which is extremely critical for path planning and obstacle avoidance. With this information, the robot can compute and apply corrective commands in real-time to avoid collision and subsequent damage. Future works will include sensor design optimization and an automated calibration scheme for the system to further improve its sensing accuracy. Eventually, the compact sensing system will be equipped into the spherical robot platform and the object avoidance algorithm will also be integrated accordingly.

## References


[1] R. Chase and A. Pandya, "A review of active mechanical driving principles of spherical robots", *Robotics*, vol. 1, pp. 3-23, 2012.

[2] R. H. Armour and J. F. Vincent, "Rolling in nature and robotics: a review", *Journal of Bionic Engineering*, vol. 3, pp. 195-208, 2006.

[3] X. Niu, A. P. Suherlan, G. S. Soh, S. Foong, K. Wood, and K. Otto, "Mechanical development and control of a miniature nonholonomic spherical rolling robot", *International Conference on Control Automation Robotics & Vision (ICARCV)*, pp. 1923-1928, 2014.

[4] W.-H. Chen, C.-P. Chen, J.-S. Tsai, J. Yang, and P.-C. Lin, "Design and implementation of a ball-driven omnidirectional spherical robot", *Mechanism and Machine Theory*, vol. 68, pp. 35-48, 2013.

[5] M. Seeman, M. Broxvall, A. Saffiotti, and P. Wide, "An autonomous spherical robot for security tasks", *Proceedings of the 2006 IEEE International Conference on Computational Intelligence for Homeland Security and Personal Safety*, pp. 51-55,2006.

[6] V. A. Ajay, A. P. Suherlan, G. S. Soh, S. Foong, K. Wood, and K. Otto, "Localication and trajectory tracking of an autonomous spherical rolling robot using IMU and odometry", *Proceedings of the ASME 2015 International Design Engineering Technical Conferences & Mechanisms and Robotics Conference (IDETC/MECH)*, August 2-5 2015, Boston, USA.

[7] X. Lin, S. Guo, K. Tanaka, and S. Hata, "Underwater experiments of a water-jet-based spherical underwater robot", *2011 International Conference on Mechatronics and Automation (ICMA)*, pp. 738-742, 2011.

[8] D. Preethichandra and K. Shida, "A simple interface circuit to measure very small capacitance changes in capacitive sensors", *IEEE Transactions on Instrumentation and Measurement*, vol. 50, no.6, pp. 1583-1586, 2001.

[9] S. Liu, Q. Meng, Y. Luo, and D. Tang, "The precise mathematical model of the capacitance sensor of unspecific form", *Proceedings of the 2009 IEEE International Conference on Mechatronics and Automation*, pp. 4100-4104, 2009.

[10] F. Wu, S. K. Moon, and H. Son, "Orientation measurement based on magnetic inductance by the extended distributed multi-pole model", *Sensors*, vol. 14, pp. 11504-11521, 2014.

[11] Y. Deng and X. Liu, "Electromagnetic Imaging Methods for Nondestructive Evaluation Applications", *Sensors*, vol. 11, no.12, pp. 11774-11808, 2011.

[12] N. Misron, L. Q. Ying, R. N. Firdaus, N. Abdullah, N. F. Mailah, and H. Wakiwaka, "Effect of Inductive Coil Shape on Sensing Performance of Linear Displacement Sensor Using Thin Inductive Coil and Pattern Guide", *Sensors*, vol. 11, no.11, pp. 10522-10533, 2011.

[13] Inductive proximity sensir, EV series, Keyence. Available: http://www.keyence.com.sg/products/sensor/proximity/ev/index.jsp

[14] K.-M. Lee and M. Li, "Magnetic field localization method for guiding visually impaired applications", *2013 IEEE/ASME International Conference on Advanced Intelligent Mechatronics (AIM)*, pp. 542-547, 2013.

[15] D. V. Lee and S. A. Velinsky, "Analysis and experimental verification of a three-dimensional noncontacting angular motion sensor", *IEEE/ASME Transactions on Mechatronics*, vol. 12, pp. 612-622, 2007.

[16] K.-M. Lee, M. Li, and C.-Y. Lin, "A novel way-finding method based on geomagnetic field effects and magnetic tensor measurements for visually impaired users", *2015 IEEE International Conference on Advanced Intelligent Mechatronics (AIM)*, pp. 232-237, 2015.